

1           On the properties of a negative-ion TPC prototype  
2                           with GridPix readout

3           C. Ligtenberg<sup>a,\*</sup>, M. van Beuzekom<sup>a</sup>, Y. Bilevych<sup>b</sup>, K. Desch<sup>b</sup>,  
4           H. van der Graaf<sup>a</sup>, F. Hartjes<sup>a</sup>, K. Heijhoff<sup>a,b</sup>, J. Kaminski<sup>b</sup>, P.M. Kluit<sup>a</sup>,  
5           N. van der Kolk<sup>a</sup>, G. Raven<sup>a</sup>, J. Timmermans<sup>a</sup>

6           <sup>a</sup>*Nikhef, Science Park 105, 1098 XG Amsterdam, The Netherlands*

7           <sup>b</sup>*Physikalisches Institut, University of Bonn, Nussallee 12, 53115 Bonn,*  
8                           *Germany*

---

9   **Abstract**

10 The performance of a GridPix detector to read out a negative ion TPC was stud-  
11 ied using a module with four GridPix chips that are based on the Timepix3 pixe-  
12 lated readout ASIC. The quad module dimensions are 39.6 mm × 28.38 mm, and  
13 the maximum drift distance is 40 mm. The TPC is operated using a 93.6/5.0/1.4  
14 gas mixture (by volume) of Ar/iC<sub>4</sub>H<sub>10</sub>/CS<sub>2</sub> with a small amount of oxygen and  
15 water vapour at a pressure of 1030 mbar and a temperature of 297 K. Tracks  
16 were produced by a pulsed N<sub>2</sub> laser. The GridPix chips are sensitive to single  
17 drift ions, and allow for the determination of the drift distance using the veloc-  
18 ities of the different ion species. The 1.56 ns time resolution of the Timepix3  
19 chips allows for a precise determination of the drift properties in the longi-  
20 tudinal direction. The measured mobility of majority ion charge carriers is  
21  $(1.391 \pm 0.003) \text{ cm}^2/\text{V/s}$ . Using the high granularity pixel readout, the trans-  
22 verse and longitudinal diffusion coefficients were measured to correspond to an  
23 effective thermal diffusion temperature of 314 K and 384 K respectively. For  
24 429 detected ions, the precision on the absolute drift distance is expected to be  
25 1.33 mm for a mean drift distance of 20 mm.

26 *Keywords:* Micromegas, gaseous pixel detector, micro-pattern gaseous  
27 detector, Timepix, GridPix, negative ion time projection chamber

---

28 **1. Introduction**

29 In a negative ion Time Projection Chamber (TPC), ionisation charge is  
30 transported to the readout plane by negatively charged ions instead of elec-  
31 trons, thereby reducing the diffusion down to the thermal limit [1]. The TPC  
32 detects ionisation from interactions in the gas of the TPC. The primary ionisa-  
33 tion electrons are captured by the highly electronegative CS<sub>2</sub> gas component,  
34 and the ions formed drift to the anode in the electric field. The track position  
35 resolution depends on the electron capture length, and the transport properties

---

\*Corresponding author. Telephone: +31 20 592 2000  
Email address: c.ligtenb@nikhef.nl (C. Ligtenberg)  
*Preprint submitted to Elsevier*

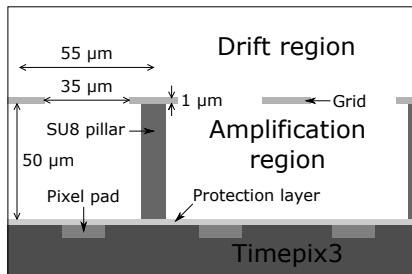


Figure 1: Schematic drawing of the cross-section of a GridPix detector, with some of the components and dimensions indicated.

36 of the gas. In the high field amplification region near the anode, the electrons  
 37 detach and an avalanche occurs which is detected by the readout electronics.

38 Negative ion TPCs can be used for directional dark matter searches. For  
 39 example, in the Drift IId experiment [2] a negative ion TPC was operated using a  
 40 low pressure 30:10 Torr  $\text{CF}_4:\text{CS}_2$  gas mixture. It was demonstrated that when  
 41 oxygen was present in the gas mixture, extra species of ions called minority  
 42 carriers with a larger mobility were created [3]. From the difference in arrival  
 43 time of the different ion species at the readout plane, the absolute position in  
 44 the drift direction was reconstructed without the need of knowing the event  
 45 time in the detector [4].

46 In this paper an exploratory study of GridPix technology to read out a  
 47 negative ion TPC is presented. A GridPix consists of a CMOS pixel chip with  
 48 integrated amplification grid added by MEMS postprocessing techniques [5, 6].  
 49 GridPix detectors based on the Timepix chip were extensively studied as TPC  
 50 readouts for a future collider experiment [7] and have been used in the CERN  
 51 Axion Solar Telescope [8], see also [9] for an overview of applications. However,  
 52 the original Timepix chip has a limited readout rate, and cannot simultaneously  
 53 record the time of arrival and the amount of detected charge. This has been  
 54 overcome by the next generation GridPix [10] based on the Timepix3 [11] chip.

55 Recently a quad module with four Timepix3 based GridPix chips was devel-  
 56 oped for a future collider experiment [12]. The Timepix3 chip can be operated  
 57 with a low threshold of  $515 e^-$ , and has a low equivalent noise charge of about  
 58  $70 e^-$ . The GridPix TPC readout is sensitive to single charge carriers, and has  
 59 a fine granularity of  $55 \mu\text{m} \times 55 \mu\text{m}$ . Because of this fine granularity and the  
 60 low diffusion of ions, a negative ion TPC with GridPix readout can provide an  
 61 excellent spatial resolution without a magnetic field. This first investigation  
 62 focuses on the operation of the quad module in an already existing setup at  
 63 atmospheric pressure.

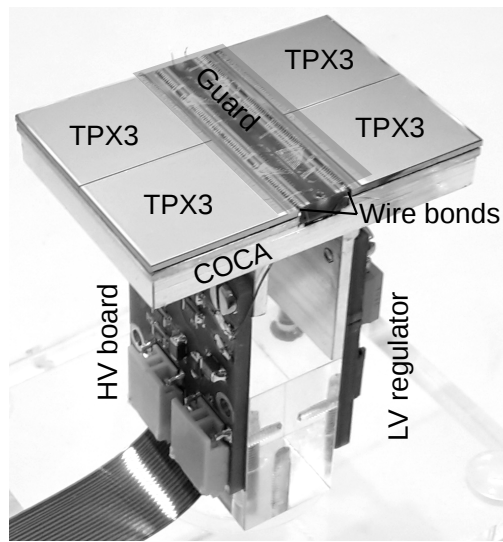


Figure 2: Picture of the quad module with four Timepix3 GridPixes (TPX3) mounted on a cold carrier plate (COCA). The central guard was not yet installed to show the underlying wire bond PCB, and its operating position is indicated with a transparent rectangle. On the right the Low Voltage (LV) regulator is partially hidden behind the aluminium mechanical support, and on the left the High Voltage (HV) board and the flexible Kapton cable are visible. This picture was previously published in [12].

## 64 2. Quad detector

### 65 2.1. Gridpix

66 The GridPix is based on the Timepix3 chip [11], which has  $256 \times 256$  pixels  
67 with a pitch of  $55 \mu\text{m} \times 55 \mu\text{m}$ . On the surface of the chip a  $4 \mu\text{m}$  thick silicon-  
68 rich silicon nitride resistive protection layer is deposited in order to prevent  
69 damage to the readout electronics from discharges of the grid. Silicon-rich silicon  
70 nitride is regular silicon nitride ( $\text{Si}_3\text{N}_4$ ) doped with extra silicon to make it  
71 conductive. On top of the protection layer,  $50 \mu\text{m}$  high pillars of the epoxy-  
72 based negative photoresist SU8 support a  $1 \mu\text{m}$  thick aluminium grid with  $35 \mu\text{m}$   
73 diameter circular holes aligned to the pixels. Some of the components and  
74 dimensions are schematically drawn in Figure 1. The Timepix3 chip can measure  
75 a precise Time of Arrival (ToA) using a 640 MHz TDC. In addition for every  
76 hit a time over threshold (ToT) is measured, which can be converted into a  
77 detected charge by test pulse calibrations. The Timepix3 chip has a data driven  
78 readout, and is connected to a speedy pixel detector readout (SPIDR) board at  
79 a speed of 160 Mbps [13].

### 80 2.2. Quad module

81 The quad module shown in Figure 2, consists of four GridPix chips and is  
82 optimised for a high fraction of sensitive area of 68.9%. The external dimensions  
83 are  $39.6 \text{ mm} \times 28.38 \text{ mm}$  and it can be tiled to cover arbitrarily large areas. The  
84 four chips which are mounted on a cooled base plate (COCA), are connected  
85 with wire bonds to a common central 6 mm wide PCB. A 10 mm wide guard  
86 electrode is placed over the wire bonds 1.1 mm above the aluminium grids, in  
87 order to prevent field distortions of the electric drift field. The guard is the  
88 main inactive area, and its dimensions are set by the space required for the  
89 wire bonds. On the back side of the quad module, the PCB is connected to  
90 a low voltage regulator. The aluminium grids of the GridPixes are connected  
91 by  $80 \mu\text{m}$  insulated copper wires to a high voltage (HV) filtering board. The  
92 module consumes about 8 W of power of which 2 W is used in the LV regulator.

### 93 2.3. Experimental setup

94 Eight quad modules were embedded in a box, resulting in a total of 32 chips.  
95 A schematic 3-dimensional drawing of the detector is shown in Figure 3. When  
96 the measurements were taken, one single quad module with four chips could be  
97 read out per SPIDR board. Hardware to simultaneously read out multiple quad  
98 modules with one SPIDR board is under development. A schematic drawing  
99 of the setup is shown in Figure 4. The internal dimensions of the box are  
100 79 mm along the  $x$ -axis, 192 mm along the  $y$ -axis, and 53 mm along the  $z$ -axis  
101 (drift direction), and it has a maximum drift length (distance between cathode  
102 and readout anode) of 40 mm. The drift field is shaped by a series of parallel  
103 CuBe field wires of  $50 \mu\text{m}$  diameter with a wire pitch of 2 mm and guard strips  
104 are located on all of the four sides of the active area. In addition, six guard  
105 wires are suspended over the direct boundaries of the chips, because the chip

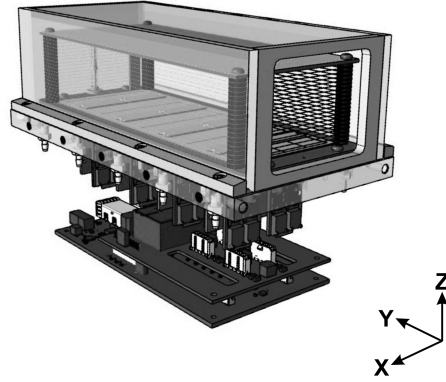


Figure 3: Schematic 3-dimensional render of the 8-quad module detector for illustration purposes.

106 edges are at a ground potential, which would otherwise distort the electric drift  
 107 field. The wires are located at a distance of 1.15 mm from the grid planes, and  
 108 their potential is set to the potential at this drift distance. The box has one  
 109 Kapton window and three optical glass windows (type H-K9L) to facilitate laser  
 110 measurements.

111 The gas volume of 780 ml is continuously flushed with a 93.6/5.0/1.4 gas mix-  
 112 ture (by volume) of Ar/ $i\text{C}_4\text{H}_{10}$ / $\text{CS}_2$  at atmospheric pressure. The gas is argon  
 113 based, because the setup is also used for research on TPCs with an argon based  
 114 gas for future colliders. The isobutane gas was added as a quencher to absorb  
 115 UV photons produced in the avalanches, and the  $\text{CS}_2$  concentration is chosen  
 116 high enough to capture electrons shortly after the ionisation ( $\lesssim 200 \mu\text{m}$ ). This  
 117 upper limit on the attachment distance can be derived from the measurements

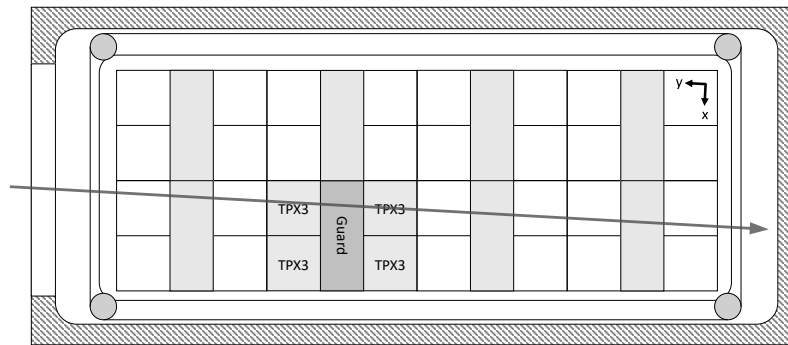


Figure 4: Schematic drawing of the 8-quad module detector with one quad in operation. The laser track direction is shown in purple.

118 shown later in Figure 9. The oxygen content is measured with a Mettler-Toledo  
 119 trace oxygen meter, sensor InPro6950i and the humidity is with a Sensirion  
 120 sensor type SHT85. A small amount of oxygen (650 ppm–1150 ppm) and water  
 121 vapour (about 4000 ppm) are present in the drift volume because of diffusion  
 122 and outgassing of some of the materials. A few ppb of tetra-methyl-phenylene-  
 123 diamine (TMPD) molecules are added to enhance laser ionisation in the gas  
 124 [14]. The TMPD was added through sublimation by directing the inflowing gas  
 125 through a tube containing the solid TMPD grains. Once introduced, a notice-  
 126 able concentration can remain in the setup for at least months under normal  
 127 conditions. During data taking, the temperature was 297 K and the pressure  
 128 was 1030 mbar. The experimental parameters are summarised in Table 1.

129 An amplification field strength  $E_{\text{amplification}}$  of 76 kV/cm is achieved in the  
 130 50  $\mu\text{m}$  wide gap by setting the grid voltage to  $-380\text{ V}$ . The pixel pads are  
 131 normally at zero potential. A hit is registered if the charge on a pixel pad  
 132 is above the threshold set to about  $515\text{ e}^-$ . The mean collected charge of the  
 133 selected hits is about  $1000\text{ e}^-$ . The gain is approximately 1000, and the single ion  
 134 detection efficiency is expected to be 60%. A higher gain and single ion detection  
 135 efficiency can be achieved by increasing the amplification field strength.

136 Tracks of ionisation are created by a pulsed 337 nm  $\text{N}_2$  laser at a rate of  
 137 2.5 Hz with a pulse duration of 1 ns [14]. This laser is operated using the MOPA  
 138 (Master Oscillator Power Amplifier) principle to obtain a beam near the diffrac-  
 139 tion limit. The parallel beam can accurately be directed in the gas volume by  
 140 means of two remotely controlled stages.

141 Data was taken using the data-driven mode of the Timepix3 chip in a series  
 142 of nine automated experimental runs. The time of the laser pulse was added to  
 143 the pixel data stream. During a run, the drift field was set to a specific strength  
 144 and the beam was positioned at six different drift distances 6 mm apart and at  
 145 four different  $x$ -positions. Measurements of 2400 laser pulses per run are taken  
 146 in a time frame of approximately 17 minutes.

Table 1: Overview of the experimental parameters. The ranges indicate the variation over the total data taking time

Number of runs	9
Run duration	17 minutes
$E_{\text{drift}}$	100 – 500 V/cm
$E_{\text{amplification}}$	76 kV/cm
Threshold	$515\text{ e}^-$
Temperature	295.9 – 297.0 K
Pressure	1030 – 1029 mbar
Oxygen concentration	650 – 1150 ppm
Water vapour concentration	$\sim 4000\text{ ppm}$

147 **3. Analysis**

148 In the analysis the laser position is compared to the reconstructed position  
 149 from the quad detector. The laser track is defined by the recorded stage position  
 150 as a line parallel to the  $y$ -axis. The per pulse variations are smaller than  $15\ \mu\text{m}$ .  
 151 The recorded stage position is taken as the reference to which the four chips  
 152 are aligned by rotation in two dimensions, and shifts in the two dimensions  
 153 perpendicular to the laser beam. The position of detected ionisation in the  
 154 pixel plane is a direct translation from the pixels column ( $x$ -direction) and row  
 155 number ( $y$ -direction). To reduce noise, only hits with a time over threshold  
 156 above  $0.1\ \mu\text{s}$  are considered. A time over threshold of  $0.1\ \mu\text{s}$  corresponds to  
 157 a charge close to the threshold of  $515\ e^-$ . From the known laser pulse time,  
 158 the  $z$ -position can be calculated as the product of the measured drift time  $t$   
 159 and the drift velocity  $v_{\text{drift}}$ . To remove noise from scattered laser light hitting  
 160 the readout directly, hits between  $1\ \mu\text{s}$  before and  $1\ \mu\text{s}$  after the laser pulse are  
 161 removed. All of these cuts are applied in the entire analysis below. To clean  
 162 up further the data set for diffusion measurements only, in section 4.3 hits are  
 163 required to be within  $2\ \text{mm}$  of a laser track in the  $x$ -direction and to be within  
 164  $5\ \text{mm}$  of the laser track in the  $z$ -direction. The alignment and the measurement  
 165 of the drift velocity is an iterative process.

166 An example of a resulting drift time spectrum is shown in Figure 5 for the  
 167 run at a drift field strength  $E_{\text{drift}}$  of  $300\ \text{V/cm}$ . Other experiments using a  
 168  $30:10:1$  Torr  $\text{CF}_4:\text{CS}_2:\text{O}_2$  gas mixture could distinguish three different minority  
 169 carriers as separate peaks in the drift time spectrum [3]. In contrast, in our  
 170 measurements only one secondary peak can be found, which is slightly broader  
 171 than the primary one. This could be due to e.g. overlapping drift time distribu-  
 172 tions, the much lower oxygen concentration, or the much higher water vapour  
 173 concentration in our gas mixture affecting the minority carrier(s) production.

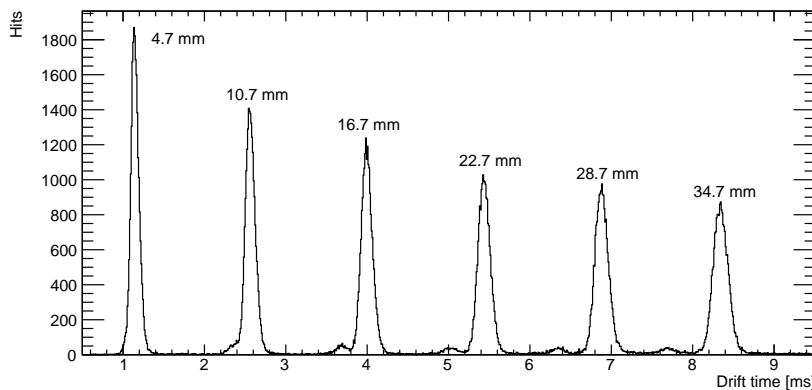


Figure 5: Drift time distribution for 400 laser pulses per  $z$ -position, annotated with the drift distance as recorded by the laser stage.

174 In order to determine the drift properties, a ‘global’ fit is made per run.  
 175 Each run corresponds to a given electric field strength. A run has measurements  
 176 taken at different drift distances. The drift time  $t$  distribution is fitted with a  
 177 combination of two Gaussian distributions per laser  $z$ -position:

$$g(t) = n_{\text{hits}} \left[ \frac{f_1}{\sigma_1 \sqrt{2\pi}} \exp\left(-\frac{(t - \mu_1)^2}{2\sigma_1^2}\right) + \frac{f_2}{\sigma_2 \sqrt{2\pi}} \exp\left(-\frac{(t - r_2 \mu_1)^2}{2\sigma_2^2}\right) + \frac{f_{\text{noise}}}{u_{\text{width}}}\right], \quad (1)$$

178 where  $n_{\text{hits}}$  is the number of hits,  $u_{\text{width}}$  is the width of a uniform distribution  
 179 related to the fitted  $t$  range and  $f_1$  is the fraction of the number of detected  
 180 ions from majority carrier(s) given by  $f_1 = 1 - f_2 - f_{\text{noise}}$ . Four parameters are  
 181 different for each drift distance, and two parameters are the same for all drift  
 182 distances. The mean time  $\mu_1$ , the standard deviation of the majority carrier  
 183 distribution  $\sigma_1$ , the standard deviation of the minority carrier(s) distribution  
 184  $\sigma_2$  and the fraction of the number of ions in the flat noise distribution  $f_{\text{noise}}$ ,  
 185 are fitted per drift distance. In the fit, the fraction of the number of ions from  
 186 minority carrier(s)  $f_2$  and the ratio of majority carrier mobility to the minority  
 187 carrier(s) mobility  $r_2$  are equal for all drift distances.

## 188 4. Performance

### 189 4.1. Number of hits

190 The mean total number of detected hits per laser pulse is 43. The number of  
 191 hits can be tuned by adjusting the laser intensity, and the spread on the number  
 192 of hits is dominated by per pulse variations of the laser intensity. In this gas, a  
 193 minimum ionising particle is expected to create about 100 ionisation pairs per  
 194 cm of which about 60 will be detected as hits per cm, because of the 60 % single  
 195 ion detection efficiency at a gain of 1000. An example event display showing  
 196 the ionisation for a single laser pulse is presented in Figure 6.

197 The GridPix is capable of detecting more than one hit per laser pulse per  
 198 pixel. The dead time per pixel for the Timepix3 chip after being hit is the  
 199 time over threshold plus 475 ns, so about 1  $\mu$ s. With a drift velocity of a few  
 200 m/s, even two hits originating from the same position can both be detected,  
 201 because they are sufficiently separated due to diffusion. In this case the number  
 202 of hits is small, and there is only a small probability of two ions arriving on  
 203 the same pixel, but for highly-ionising events the multi-hit capabilities can be  
 204 advantageous.

### 205 4.2. Drift velocity measurements

206 The average drift times for the majority and minority charge carrier(s) are  
 207 plotted as a function of the drift distance in Figure 7 for a drift field strength of  
 208 300 V/cm. The drift velocity of the minority carrier is found to be 8.1% higher  
 209 than that of the majority carrier.

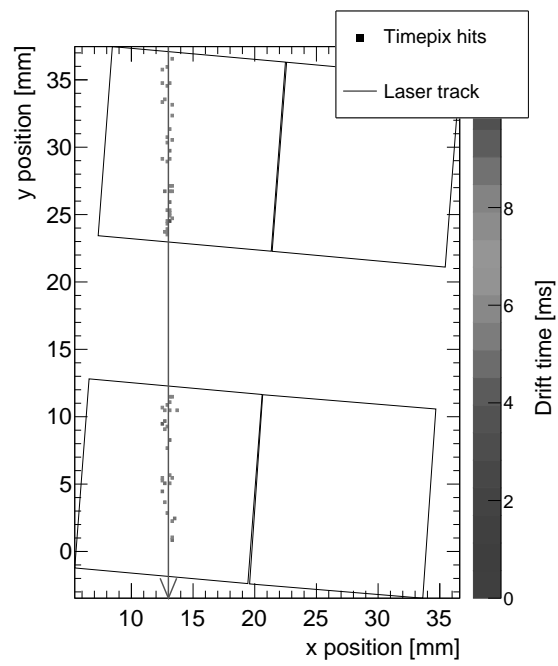


Figure 6: Example of the detected ionisation from one laser pulse with 71 hits in total. The position of the laser track (purple line) and chip edges (black outlines) are drawn in global coordinates. The pixel hits are not to scale.

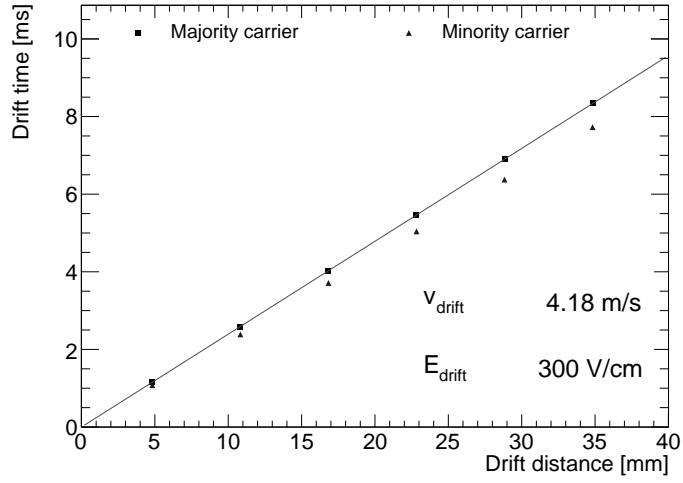


Figure 7: Drift time as a function of the drift distance for the majority and minority carriers. The statistical error is not shown, because it is negligible compared to the systematic uncertainties.

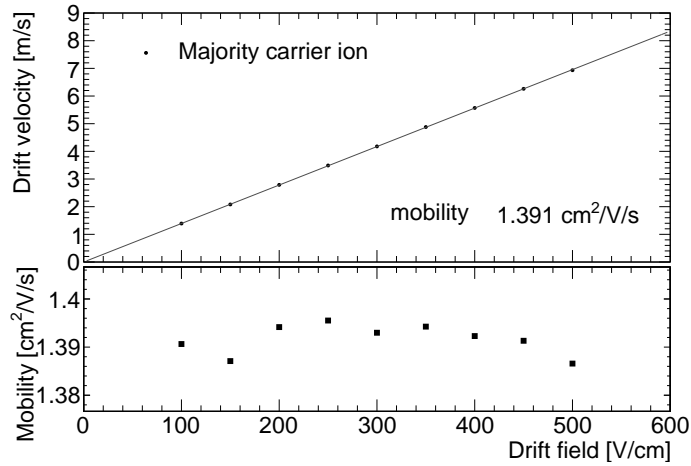


Figure 8: Drift velocity of the majority carrier ion as a function of the drift field. The mobility is acquired from a straight line fit constrained to pass through the origin (0,0). The statistical error is not shown, because it is negligible compared to the systematic uncertainties.

210 The drift velocity measurement is repeated for 9 electric field strengths in  
 211 the range 100 V/cm to 500 V/cm. The drift velocity of the majority carrier  
 212  $v_{\text{drift}}$  as function of the electric field is shown in Figure 8. The mean measured  
 213 mobility (defined as the drift velocity divided by the electric field strength) is  
 214  $(1.391 \pm 0.003) \text{ cm}^2/\text{V/s}$ . The uncertainty of the measured mobility is estimated  
 215 as the r.m.s. of the given values, and is probably dominated by fluctuations  
 216 in the (local) temperature and gas composition. Because of the unique gas  
 217 composition the mobility cannot directly be compared to the results from other  
 218 experiments. However, the mobility is the same order of magnitude as previous  
 219 measurements. Reference [1] found a mobility of  $(1220 \pm 51) \text{ cm}^2/\text{V/s mbar}$  for  
 220 a 9:1:14.5 Ar:CH<sub>4</sub>:CS<sub>2</sub> gas mixture at a pressure of 40 Torr (53 mbar), which  
 221 corresponds to a mobility of  $(1.18 \pm 0.04) \text{ cm}^2/\text{V/s}$  at a pressure of 1030 mbar.  
 222 Reference [15] found a mobility of  $0.71 \text{ cm}^2/\text{V/s}$  in a 200:500 Torr CS<sub>2</sub>:He gas  
 223 mixture.

#### 224 4.3. Diffusion measurements

225 As the ions drift towards the readout plane, they diffuse which gives them  
 226 a Gaussian spread in the longitudinal and transverse direction. The amount of  
 227 diffusion is characterised by the standard deviation of the Gaussian distribution  
 228  $\sigma_i$ , where  $i$  stands for the longitudinal direction  $z$  or the transverse direction  $x$ .  
 229 This can be expressed as

$$\sigma_i^2 = \sigma_{i0}^2 + D_i^2 z, \quad (2)$$

230 where  $\sigma_{i0}$  is the standard deviation at zero drift,  $D_i$  the diffusion coefficient,  
 231 and  $z$  the drift distance.

232 The standard deviation in the transverse direction  $\sigma_x$  is acquired from a fit of  
 233 a Gaussian function to the measured  $x$  positions of all detected ions including the  
 234 minority carrier(s) ions. In the longitudinal direction the standard deviation  $\sigma_z$   
 235 is acquired from a fit of the sum of two Gaussian functions, which represent the  
 236 contribution from the majority carrier ions, and the minority carrier(s) ions, see  
 237 Equation (1). The drift time is converted to a distance using the measured drift  
 238 velocity of the majority carrier  $v_{\text{drift}}$ . As an example, the standard deviation  
 239 as a function of drift distance for the run at a drift field strength  $E_{\text{drift}}$  of  
 240 300 V/cm is shown in Figure 9. In comparison to the systematic uncertainties,  
 241 the statistical error is negligible.

242 The constant contribution in Equation 2 is roughly independent of the elec-  
 243 tric field, and on average found to be  $\sigma_{x0} = (84 \pm 4) \mu\text{m}$  in the transverse direc-  
 244 tion which can predominantly be attributed to the laser beam width plus some  
 245 small per laser pulse variation. The laser beam is symmetric in both directions.  
 246 In the longitudinal direction  $\sigma_{z0} = (141 \pm 8) \mu\text{m}$  is measured on average over  
 247 all runs. This can predominantly be attributed to the laser beam width plus  
 248 per laser pulse variations, the spread on the distance traveled by electrons be-  
 249 fore they are captured by the CS<sub>2</sub> molecules and possible unrecognised minority  
 250 carrier(s). From these measurements it can be concluded that the attachment  
 251 distance is  $\lesssim 200 \mu\text{m}$ .

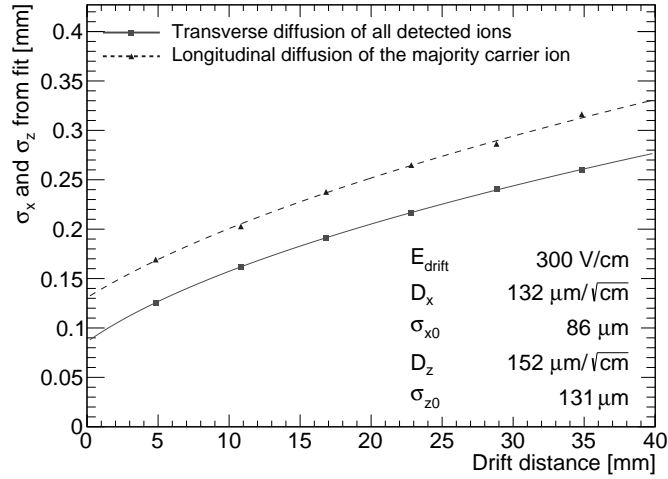


Figure 9: Standard deviation of the hit positions of all detected ions in the transverse direction, and the standard deviation of the hit positions of the majority carrier ions in the longitudinal direction. Both are shown as a function of drift distance for the run with  $E_{\text{drift}} = 300 \text{ V/cm}$ . The data is fitted with Equation (2).

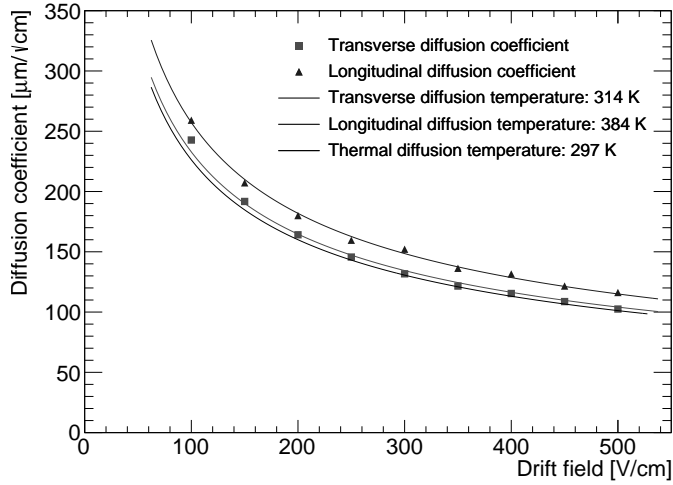


Figure 10: The longitudinal diffusion coefficient of the majority carrier ions, and the transverse diffusion of all detected ions. Both are plotted as a function of drift field  $E$ , and fitted with Equation (3). For comparison the expectation for thermal diffusion is shown.

252 The diffusion coefficient depends on the electric field strength, and the mea-  
 253 surements are shown in Figure 10. Because of the much larger systematic un-  
 254 certainties, the statistical errors are neglected. At low drift field strengths, the  
 255 ions have thermal energy and the diffusion coefficient can be expressed as

$$D_{\text{thermal}} = \sqrt{\frac{2k_{\text{B}}T}{eE}}, \quad (3)$$

256 where  $k_{\text{B}}$  is the Boltzmann constant,  $T$  is the temperature of the gas,  $e$  is the  
 257 charge of the ion, and  $E$  is the electric field strength (see e.g. [16]). Both the  
 258 transverse and longitudinal diffusion coefficients are fitted with Equation (3)  
 259 with the temperature  $T$  as a free parameter. The transverse diffusion corre-  
 260 sponds to an effective temperature of 314 K, which is slightly above the gas  
 261 temperature. The effective temperature of the longitudinal diffusion is rather  
 262 high, 384 K. This can possibly be explained by unrecognised minority carrier(s).  
 263 A simple thermal model with a  $1/\sqrt{E_{\text{drift}}}$  dependence describes the data well.

264 In other experiments using a low pressure  $\text{CS}_2$  gas, the longitudinal diffusion  
 265 is found to be in agreement with the thermal values [17]. In a 500 Torr He and  
 266 200 Torr  $\text{CS}_2$  gas mixture, longitudinal diffusion coefficients slightly below to  
 267 the thermal values are found [15].

#### 268 4.4. Reconstruction of drift distance

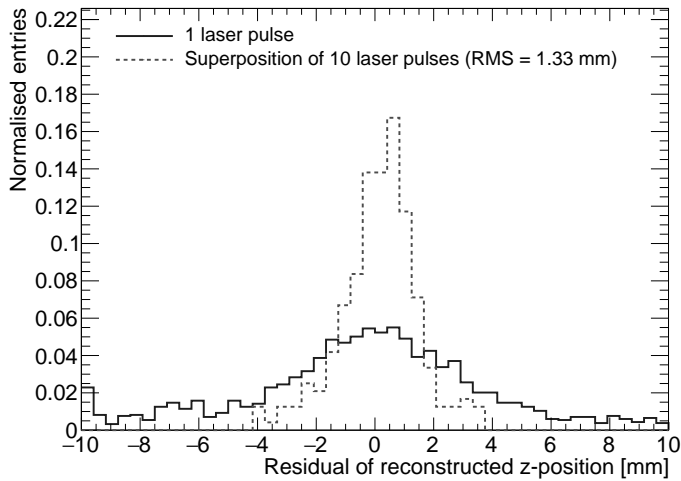


Figure 11: Residual of reconstructed  $z$ -position for single laser pulses and a superposition of ten laser pulses for all six drift distances (4.7 mm, 10.7 mm, 16.7 mm, 22.7 mm, 28.7 mm, and 34.7 mm).

269 The difference in drift velocity between the majority carrier and minority  
 270 carrier(s) ions can be used to reconstruct the absolute drift distance. Previously,

271 this technique was demonstrated in a 30:10:1 Torr CS<sub>2</sub>:CF<sub>4</sub>:O<sub>2</sub> gas mixture with  
272 a spread on the reconstructed drift distance of  $\pm 2$  cm for a mean drift distance  
273 of about 25 cm [4]. A precision of 16 mm was achieved using a similar technique  
274 using an SF<sub>6</sub> gas [18]. Besides the difference in time of arrival between the  
275 majority carrier and minority carrier(s), the detected spread due to diffusion  
276 can be used to determine the drift distance. A precision of 1 cm was achieved  
277 by measuring the transverse spread for 0.8 cm-long alpha track segments in a  
278 70:30 He:CO<sub>2</sub> gas mixture at atmospheric pressure [19].

279 Here, fiducialisation is applied to data from the run at the largest drift  
280 field of 500 V/cm which gives the best signal peak separation, and also has the  
281 highest oxygen concentration of about 1150 ppm. About 4.4% of the hits are  
282 attributed to the minority carrier(s), whose mobility is 8.1% higher than that  
283 of the majority carrier.

284 The reconstruction proceeds by performing per event a binned maximum  
285 likelihood fit of Equation (1) to the measured relative arrival time of ions from  
286 one or more laser pulses. A new parameter  $t_0$  is introduced to absorb the  
287 now unknown laser pulse time. The parameters  $f_2$ ,  $r_2$ ,  $f_{\text{noise}}$  are fixed to their  
288 previously fitted values. For  $\sigma_1$  Equation (2) is used, and  $\sigma_2$  is by approximation  
289 fixed to  $\sigma_1$ . The parameter  $\mu_1$  (the mean arrival time of the primary carrier  
290 peak) are acquired from the fit. The  $z$ -position is calculated using the measured  
291 drift velocity  $v_{\text{drift}}$ . The detected spread in the transverse direction is not utilised  
292 in the determination of the  $z$ -position.

293 By comparing the reconstructed  $z$ -position to the  $z$ -position of the laser  
294 stage for all six drift distances (4.7 mm, 10.7 mm, 16.7 mm, 22.7 mm, 28.7 mm,  
295 and 34.7 mm), the residual shown in Figure 11 is obtained. There are 2401 laser  
296 pulses with a mean number of 43 detected ions and 240 superpositions of ten  
297 laser pulses with a total mean number of 429 ions. From a single laser pulse, on  
298 average 43 ions are detected and 76 % of the laser pulses fall within the  $\pm 10$  mm  
299 range. The determined  $z$ -position has a rather large spread, because very few  
300 minority carrier(s) ions are detected. In order to estimate the performance for a  
301 larger number of ions, a superposition of ten laser pulses at the same  $z$ -position  
302 is made by shifting their arrival times by the time difference between the laser  
303 pulses. From this we acquire emulated pulses with a mean total number of 429  
304 detected ions of which about 19 ions are attributed to the minority carrier(s).  
305 The resulting r.m.s. is 1.33 mm for 239 out of the 240 combined laser pulses for  
306 a mean drift distance of 20 mm. For one entry the reconstructed  $z$ -position is  
307 off by 14 mm, and the r.m.s. is 1.62 mm if it is included as well.

## 308 5. Conclusions and outlook

309 The performance of a GridPix detector to readout a negative ion TPC was  
310 studied using a quad module with four Timepix3 based GridPix chips. The TPC  
311 is operated using a 93.6/5.0/1.4 gas mixture (by volume) of Ar/iC<sub>4</sub>H<sub>10</sub>/CS<sub>2</sub>  
312 with a small amount of oxygen and water vapour at a pressure of 1030 mbar  
313 and a temperature of 297 K. Tracks were produced by a pulsed N<sub>2</sub> laser. The  
314 1.56 ns time resolution of the Timepix3 chips allows for a precise determination

315 of the drift properties in the longitudinal direction. The measured ion mobility  
316 for the majority carrier ions is  $(1.391 \pm 0.003) \text{ cm}^2/\text{V}/\text{s}$ . Using the high granu-  
317 larity pixel readout, the transverse and longitudinal diffusion coefficients were  
318 measured to correspond to an effective thermal diffusion temperature of 314 K  
319 and 384 K respectively. A simple thermal model with a  $1/\sqrt{E_{\text{drift}}}$  dependence  
320 describes the data well. This confirms the expected low diffusion coefficient for  
321 ions. Furthermore, the GridPix has an efficiency of approximately 60% to detect  
322 single drift ions. This can be improved by operating the device at a higher gain.  
323 By using also the relative arrival time of 429 detected ions with a mean drift  
324 distance of 20 mm, the absolute  $z$ -position can be measured with an expected  
325 precision of 1.33 mm.

326 In the future, a GridPix TPC readout might be of interest to directional  
327 dark matter experiments [20], because it provides a highly efficient detection  
328 of single electrons with an excellent time and spatial resolution. By optimizing  
329 the gas choice and maximizing the number of minority carriers, the absolute  
330  $z$  position resolution can be further improved. The often desired operation  
331 at low pressure can be investigated in combination with a GridPix readout.  
332 For these experiments gas mixtures containing  $\text{SF}_6$  have some advantages [17],  
333 and can also be studied for operation with a GridPix readout. Alternatively,  
334 for operation around atmospheric pressure replacing argon with the lighter he-  
335 lium could increase nuclear recoils lengths important for directional dark matter  
336 searches[1, 21].

337 All in all, the fine granularity and high timing precision of the GridPix TPC  
338 readout in combination with the capability to detect single ions, provide an  
339 excellent position resolution in the longitudinal and transverse direction.

## 340 Acknowledgements

341 This research was funded by the Netherlands Organisation for Scientific Re-  
342 search NWO. The authors want to acknowledge the support of the mechanical  
343 and electronics departments at Nikhef.

## 344 References

- 345 [1] C. Martoff, D. Snowden-Ifft, T. Ohnuki, N. Spooner, M. Lehner, Suppress-  
346 ing drift chamber diffusion without magnetic field, Nucl. Instrum. Meth. A  
347 440 (2000) 355–359. doi:10.1016/S0168-9002(99)00955-9.
- 348 [2] J. Battat, et al., Low Threshold Results and Limits from the DRIFT  
349 Directional Dark Matter Detector, Astropart. Phys. 91 (2017) 65–74.  
350 arXiv:1701.00171, doi:10.1016/j.astropartphys.2017.03.007.
- 351 [3] D. P. Snowden-Ifft, Discovery of Multiple, Ionization-Created Anions in  
352 Gas Mixtures Containing  $\text{CS}_2$  and  $\text{O}_2$  (8 2013). arXiv:1308.0354.

- 353 [4] J. Battat, et al., First background-free limit from a directional dark matter  
354 experiment: results from a fully fiducialised DRIFT detector, *Phys. Dark*  
355 *Univ.* 9-10 (2015) 1–7. [arXiv:1410.7821](https://arxiv.org/abs/1410.7821), [doi:10.1016/j.dark.2015.06.](https://doi.org/10.1016/j.dark.2015.06.001)  
356 001.
- 357 [5] P. Colas, A. P. Colijn, A. Fornaini, Y. Giomataris, H. van der Graaf,  
358 E. H. M. Heijne, X. Llopart, J. Schmitz, J. Timmermans, J. L. Visschers,  
359 The readout of a GEM- or micromegas-equipped TPC by means of the  
360 Medipix2 CMOS sensor as direct anode, *Nucl. Instrum. Meth. A* 535 (2004)  
361 506–510. [doi:10.1016/j.nima.2004.07.180](https://doi.org/10.1016/j.nima.2004.07.180).
- 362 [6] M. Campbell, M. Chefdeville, P. Colas, A. P. Colijn, A. Fornaini,  
363 Y. Giomataris, H. van der Graaf, E. H. M. Heijne, P. Kluit, X. Llopart-  
364 Cudie, J. Schmitz, J. Timmermans, J. L. Visschers, Detection of single elec-  
365 trons by means of a micromegas-covered MediPix2 pixel CMOS readout cir-  
366 cuit, *Nucl. Instrum. Meth. A* 540 (2005) 295–304. [arXiv:physics/0409048](https://arxiv.org/abs/physics/0409048),  
367 [doi:10.1016/j.nima.2004.11.036](https://doi.org/10.1016/j.nima.2004.11.036).
- 368 [7] M. Lupberger, Y. Bilevych, H. Blank, D. Danilov, K. Desch, A. Hamann,  
369 J. Kaminski, W. Ockenfels, J. Tomtschak, S. Zigann-Wack, Toward the  
370 Pixel-TPC: Construction and Operation of a Large Area GridPix Detector,  
371 *IEEE Trans. Nucl. Sci.* 64 (5) (2017) 1159–1167. [doi:10.1109/TNS.2017.](https://doi.org/10.1109/TNS.2017.2689244)  
372 2689244.
- 373 [8] C. Krieger, J. Kaminski, M. Lupberger, K. Desch, A GridPix-based X-ray  
374 detector for the CAST experiment, *Nucl. Instrum. Meth. A* 867 (2017)  
375 101–107. [doi:10.1016/j.nima.2017.04.007](https://doi.org/10.1016/j.nima.2017.04.007).
- 376 [9] J. Kaminski, Y. Bilevych, K. Desch, C. Krieger, M. Lupberger, GridPix de-  
377 tectors – introduction and applications, *Nucl. Instrum. Meth. A* 845 (2017)  
378 233–235. [doi:10.1016/j.nima.2016.05.134](https://doi.org/10.1016/j.nima.2016.05.134).
- 379 [10] C. Ligtenberg, et al., Performance of a GridPix detector based on the  
380 Timepix3 chip, *Nucl. Instrum. Meth. A* 908 (2018) 18–23. [arXiv:1808.](https://arxiv.org/abs/1808.04565)  
381 04565, [doi:10.1016/j.nima.2018.08.012](https://doi.org/10.1016/j.nima.2018.08.012).
- 382 [11] T. Poikela, J. Plosila, T. Westerlund, M. Campbell, M. De Gaspari,  
383 X. Llopart, V. Gromov, R. Kluit, M. van Beuzekom, F. Zappon,  
384 V. Zivkovic, C. Brezina, K. Desch, Y. Fu, A. Kruth, Timepix3: a 65K  
385 channel hybrid pixel readout chip with simultaneous ToA/ToT and sparse  
386 readout, *JINST* 9 (05) (2014) C05013.  
387 URL <http://stacks.iop.org/1748-0221/9/i=05/a=C05013>
- 388 [12] C. Ligtenberg, et al., Performance of the GridPix detector quad, *Nucl.*  
389 *Instrum. Meth. A* 956 (2020) 163331. [arXiv:2001.01540](https://arxiv.org/abs/2001.01540), [doi:10.1016/](https://doi.org/10.1016/j.nima.2019.163331)  
390 [j.nima.2019.163331](https://doi.org/10.1016/j.nima.2019.163331).
- 391 [13] B. van der Heijden, J. Visser, M. van Beuzekom, H. Boterenbrood, S. Kulis,  
392 B. Munneke, F. Schreuder, SPIDR, a general-purpose readout system for

- 393 pixel ASICs, JINST 12 (02) (2017) C02040. doi:10.1088/1748-0221/12/  
394 02/C02040.
- 395 [14] F. Hartjes, A diffraction limited nitrogen laser for detector calibration in  
396 high energy physics, Ph.D. thesis, University of Amsterdam (1990).  
397 URL [https://www.nikhef.nl/pub/services/biblio/theses\\_pdf/  
398 thesis\\_F\\_Hartjes.pdf](https://www.nikhef.nl/pub/services/biblio/theses_pdf/thesis_F_Hartjes.pdf)
- 399 [15] C. Martoff, R. Ayad, M. Katz-Hyman, G. Bonvicini, A. Schreiner, Negative  
400 ion drift and diffusion in a TPC near 1 bar, Nucl. Instrum. Meth. A 555  
401 (2005) 55–58. arXiv:physics/0406114, doi:10.1016/j.nima.2005.08.  
402 103.
- 403 [16] W. Blum, L. Rolandi, W. Riegler, Particle detection with drift cham-  
404 bers, Particle Acceleration and Detection, Springer, 2008. doi:10.1007/  
405 978-3-540-76684-1.  
406 URL <https://www.springer.com/gp/book/9783540766834>
- 407 [17] N. Phan, R. Lafler, R. Lauer, E. Lee, D. Loomba, J. Matthews, E. Miller,  
408 The novel properties of SF<sub>6</sub> for directional dark matter experiments, JINST  
409 12 (02) (2017) P02012. arXiv:1609.05249, doi:10.1088/1748-0221/12/  
410 02/P02012.
- 411 [18] T. Ikeda, T. Shimada, H. Ishiura, K. Nakamura, T. Nakamura, K. Miuchi,  
412 Development of a Negative Ion Micro TPC Detector with SF<sub>6</sub> Gas for the  
413 Directional Dark Matter Search (4 2020). arXiv:2004.09706.
- 414 [19] P. Lewis, S. Vahsen, I. Seong, M. Hedges, I. Jaegle, T. Thorpe, Absolute  
415 Position Measurement in a Gas Time Projection Chamber via Transverse  
416 Diffusion of Drift Charge, Nucl. Instrum. Meth. A 789 (2015) 81–85. arXiv:  
417 1410.1131, doi:10.1016/j.nima.2015.03.024.
- 418 [20] S. E. Vahsen, C. A. J. O’Hare, W. A. Lynch, N. J. C. Spooner, E. Barac-  
419 chini, P. Barbeau, J. B. R. Battat, B. Crow, C. Deaconu, C. Eldridge, A. C.  
420 Ezeribe, M. Ghrear, D. Loomba, K. J. Mack, K. Miuchi, F. M. Mouton,  
421 N. S. Phan, K. Scholberg, T. N. Thorpe, Cygnus: Feasibility of a nuclear  
422 recoil observatory with directional sensitivity to dark matter and neutrinos  
423 (2020). arXiv:2008.12587.
- 424 [21] E. Baracchini, G. Cavoto, G. Mazzitelli, F. Murtas, F. Renga, S. Tomassini,  
425 Negative Ion Time Projection Chamber operation with SF<sub>6</sub> at nearly at-  
426 mospheric pressure, JINST 13 (04) (2018) P04022. arXiv:1710.01994,  
427 doi:10.1088/1748-0221/13/04/P04022.